PIV Measurements within a Water Analog Engine

D.Fetter, E. Suk, and P. Sullivan
Mechanical and Industrial Engineering
University of Toronto, Toronto, Ontario, Canada, M5S 3GS

May 27, 2000

Abstract

Cyclic flow in a water analog engine with two circular valved inlets has been investigated with Particle Image Velocimetry (PIV). A unique triggering and data collection system was developed, allowing a CCD to acquire two consecutive images at a specific crank angle. An optical water analog engine, operating at 15 RPM with a square cross-section and two circular valved inlets was constructed to simulate quasi-periodic non-stationary flow. The mean flow, RMS turbulence velocities, average Reynolds stresses, and average vorticity were determined by ensemble averaging 200 velocity fields at the 2 different measurement locations presented here. It was found that near the valves, there existed high intensity localized mixing while further downstream, the mixing was found to be spatially uniform and not as intense. The RMS turbulent quantities indicated a wider range of velocity closer to the valves than downstream. An adaptive cross correlation and validation PIV algorithm implemented by Usera (1999) was used. This algorithm improved the spatial resolution and the velocity results with respect to standard cross correlation and validation procedure.

Key Words : Turbulence, Cyclic flow, Particle Image Velocimetry(PIV), Mixing

Introduction

In-cylinder flow motion within internal combustion (IC) engines has been recognized as one of the most important factors controlling combustion (Heywood, 1988). In-cylinder flow motion has been classified as a nonstationary, quasi-periodic flow showing nonrepetitive, cycle-to-cycle variations where the flow can appear to be nearly chaotic ((Durst et al., 1992). Single point velocity measurements have been performed in engine flows using hotwire anemometry (Lancaster, 1976; Catania & Mittica, 1987) and laser Doppler anemometry (Liou & Santavicca, 1983). It is clear that there is a need to extract spatial characteristics of the flow field (Choi & Guezennec, 1999) as single point measurements do not capture the spatial dependence of this flow. Particle Image Velocimetry has allowed spatial quantities such as vorticity and strain to be extracted (Reuss et al., 1989, 1990).

The water analog engine is used as an alternative to real IC engine, as higher Reynolds numbers and thus turbulence, can be achieved at significantly lower velocities with water than with air. Ekchian and Hoult (1979) investigated steaklines at different crank angles and different speeds in a cylindrical, plexiglass piston chamber. The results indicated that the flow was highly repeatable when toroidal vortices were present. Arcoumanis et al. (1987) did a similar experiment with an optical plexiglass cylindrical engine and with a second fluid to simulate the injection of fuel to study the effect of injection on the flow structure. It was concluded that the injected fluid had a definite effect on the flow field as compared with one without injected fluid. Tthe flow structure is transformed by the jet impingement on the piston and this impingement resulted in a second toroidal vortex between the piston and the cylinder wall. Khalighi and Huebler (1988) captured streaklines using a 2W argon laser within a cylindrical dual-intake water analog engine. Khalighi (1990) found in-cylinder flow structures were strongly affected by changing the inlet/valve configurations

Trigui et al. (1994, 1996) used 3-D Particle Tracking Velocimetry (PTV) in a 4 valve pent roof engine with water as a working fluid. Image collection limited the measurement to the end of the intake stroke at BDC the operating piston speeds were 12.3 and 10.0 RPM for the water analog simulation. The results indicated the significance of integral measures (swirl and tumble ratios) in relation to the combustion process and more stable and high intensity dominant flow structures such as swirl (fluid rotation about cylinder axis) and tumble (fluid rotation normal to the cylinder axis) production with decreased cycle-to-cycle variations. Choi et al. (1996), Choi (1998) repeated the experiments for two different operating speeds (10 and 20 RPM) again with 3-D PTV elucidating the appearance of smaller scale flow patterns found for the higher operating speed. An estimation of the dispersion with 3-D PTV results was also done to provide an order of magnitude of the overall mixing characteristics (Choi & Guezennec, 1997).

Denlinger et al. (1998) performed 3-D PTV in in the same facility at 10.7 RPM, and found that small scale motions are important to the turbulent mixing while the large-scale structures store a great deal of kinetic energy which are transformed into turbulence as these structures break down.

Amsden (1993) developed KIVA to simulate air flow, fuel sprays and combustion in practical combustion such as automobile and truck engines, gas turbines and industrial furnaces. Li and Sullivan (2000) compared previous PIV measurements (Davis, 1999) with KIVA results and found good agreement between the two techniques at 20 RPM. There was some strong three-dimensionality that appeared at 40 and 60 RPM.

Sullivan et al. (1999) compared ensemble, cyclic and wavelet-based averaging within SI engines and that wavelet analysis allow better understandings of SI engine flow and ensemble averages may be inappropriate with SI engine flows because of the nonstationary behavior of the flow and an overestimation of turbulence and energy.

Experimental Setup

In the present study, the flow cell was a 100 mm x 100 mm (inside area) square glass cross section with two symmetrically located (40 mm diameter) valves that were both open 15 mm (see figure l(a)). A clearance of 20 mm used and the piston stroke was set to 5 inches. A 1/2 horsepower direct current motor was used to drive, the flow at 15 RPM.

The inlet Reynolds number exceeded 125 (based on hydraulic radius) and as suggested by Durst et al. (1989) is an indicator that transition to turbulence has occurred. The mechanism for transition was the interaction of the initial vortex with the piston wall. Distilled water was used so that no large particles were in the water before the introduction of seeding particles. Spherical (15 ℓm diameter) silver coated particles with a hollow glass core and a relative density of 1.65 were used for seeding.

A 2-D planar PIV system with an external trigger was used for the measurements. A metal obstruction on the crank wheel triggered data collection at 90 crank angle degrees (CAD). This triggered a) the camera to start a new frame b) the first laser to pulse and the second to pulse 162 ℓsec after and c) the framegrabber to capture two frames. Two measurement positions were used (Figure l(b)); 35mm and 75mm away from the top of the cylinder and located in the center. 200 sets of images were acquired at each position.

A Pulnix TM-9701 CCD camera set to asynchronous reset mode was used to capture the image sets. A BITFLOW Road Runner 44 framegrabber was connected using the RS-422 digital protocol to obtain two frames from the Pulnix TM-9701 CCD camera. VideoSavant software was used to capture the image pairs. A Continuum MINILITE dual cavity Neodyymium-Yttruim Aluminum Garnet (Nd:YAG) laser was used to produce a vertically polarized green light source at 532 nm wavelength. To create a 1 mm light sheet used to illuminate particles in the flow, a cylindrical lens of -25.4mm focal length and a spherical lens of 250mm focal length were used (see figure 1(a)). A Stanford Research Model DG535 digital/pulse generator was used to trigger the laser. Velocity fields were determined using an adaptive cross correlation PIV algorithm developed by Usera (1999).

Data Reduction

The adaptive cross correlation (ACC) procedure was developed by Westerweel (1993) and Kumar and Banerjee (1998) and is an improvement over standard cross correlation (SCC) for PIV. For the SCC, as spatial resolution increases the velocity resolution decreases as each is a function of the interrogation region size. The ACC algorithm is iterative and SCC is used as a first approximation to the velocity field. In the first iteration, the spatial and velocity resolution are determined for the initial interrogation region size. The velocity field is validated by user defined criteria, and is then used as a rough estimate of the particle displacement in the second iteration. This allows smaller interrogation region size to be used and increases the spatial resolution. In this way, the velocity resolution is limited by the interrogation area as defined in the first iteration, and the spatial resolution is limited by the smaller interrogation size as defined in the second iteration.

The validation criteria were developed by Westerweel (1993), Nogueira et al. (1997) and Adrian (1991). Westerweel (1993) defined two categories of errors, (a) Type 1 errors, where valid vectors are inappropriately rejected, and (b) Type 2 errors, spurious vectors that are inappropriately accepted, that are inversely related as acceptance criteria are made stricter or relaxed. The validation procedure used here was to initially ensure that the maximum displacement of particles did not exceed a certain amount, defined as 40% of the interrogation region size. The eye validation procedure was then performed. The algorithm starts by searching for a group of locally coherent vectors. Coherency is determined by calculating how much each vector deviates from its eight neighbours:

$$dev = \frac{\sum_i | v_i - v_o |}{\sum_i | v_i |}$$

where v_i refers to the eight closest neighboring vectors of the grid node whose velocitv is v_o. The zone grows by incorporating neighbouring nodes into a coherence zone using the same criteria for each node, Usera (1999) incorporated a method allowing elliptical regions to be defined allowing local gradients within the flowfield to be tracked. This procedure is repeated until the entire velocity field is separated into several distinct coherence zones. These zones are accepted if the number of vectors exceed a certain minimum, and has been found to be extremely effective in high vorticity regions (Nogueira et al., 1997). This is a clear improvement over the SMAV, where the SMAV procedure is a localized and non-selective criterium. If, for example, there was a small group of coherent spurious vectors, the SMAV procedure would incorrectly validate this region based on comparison to their neighbours alone. After validation of the vectors, missing points within the velocity field were linearly interpolated from the eight surrounding values (Raffel et al., 1998).

Results

The initial interrogation region size was 64 pixels yielding a maximum allowable velocity of 1.4 m/s (Adrian, 1991) where the maximum allowable velocity is 40% of the interrogation area size divided by the time separation. The maximum observed velocity was at most 1/6 of the maximum allowable velocity, which ensured that no in--plane velocity vectors were eliminated because of actual excessive displacement. The final interrogation region size was 16 pixels and yielded a final spatial resolution of 0.23 mm well under the smallest scales of motion 1 mm as suggested by Dent and Salama (1975).

The 2D velocity field PIV measurements were taken at downstream 35 mm and 75 mm from the top of the cylinder along the direction of piston motion at the center (Figure l(b)). The engine was operated at 15 RPM and the data was collected at 90 Crank Angle Degrees (CAD) after Top Dead Center (ATDC). 200 images were taken for both regions and the mean velocities were found to converge within 1% for both u and v components.

The mean and instantaneous velocity fields for 35 mm and 75 mm downstream are presented in Figure 2. At 35 mm, Figure 2(a), the mean flow is moving downstream parallel with the piston motion. At 75 mm**,** figure 2(b), the mean flow is moving at an angle with respect to the piston motion. At 35 mm (see figure l(b)), the measurement zone is downstream from the clearance between the two valves (10 mm) corresponding to 3.5 jet diameters and thus in a location close to the core of a jet. At 75 mm (7.5 jet diameters), the centre jet will interact with the wall jets at the lower and upper surfaces, causing an waviness in the mean field. This is reflected in the change in direction of the mean vectors. Instantaneous velocity fields are presented in Figure 2(c) for 35 mm and Figure 2(d) for 75 mm. In both flow fields, large scale vorticity is apparent, occurring at scales larger than the measurement region.

The histograms for the mean velocity are shown in Figure 3. At 35 mm downstream (Figure 3(a)), the mean U velocity is an order of magnitude greater than the mean V velocity (Figure 3(c)) and there is a uniform velocity distribution between 90 and 200 mm/sec. The mean V velocity at 35mm is bimodal with peaks at –3 mm/sec and 30 mm/sec, suggesting that the exiting flow oscillates vertically. At 75mm downstream (Figures 3(b) and 3(d)), the mean U and V differ by a factor of two. The mean U velocities have a quasi-Gaussian distribution between 50 and 140 mm/sec and are of lower magnitude than at 35 mm. This confirms that the initial jet dominates the center region of the flow at the first measurement position (35 mm), and other influences are acting on the flow further downstream (75 mm). The mean V velocity peaks between 35 and 50 mm/sec and is skewed slightly left. This distribution is not a result of the PIV algorithm, as Usera (1999) noted that the use of eye validation reduced pixel locking, i.e., the favoring of integer pixel displacements.

RMS turbulent velocity histograms are presented in Figure 4. Both RMS values of u' and v' at 35 mm downstream (Figure 3(a) and 3(c)) have wider variances than at 75mm downstream (Figure 3(b) and 3(d)) and a higher peak value. Thus, at 35mm, the turbulence is not homogeneous and has a wider distribution of velocitv scales than at 75 mm. From figure 5, the Reynolds stresses, $\overline{u'u'}$ and $\overline{v'v'}$, are more homogeneous at 75m . The flow has significantly mixed by 75mm as demonstrated by the greater spatial uniformity of the Reynolds stresses at this position. There is greater mixing potential at 35mm as the Reynolds stresses are of significantly greater magnitude than at 75 mm.

At 35mm, the mean vorticity field (figure 6(a)) shows that there is significant negative vorticity within this flow. with comparatively little positive vorticity (regions encompassed in white on the contour plot). Further downstream at 75mm (figure 6(b)), the vorticity has become less uniform. From figures 6(c) and 6(d), the average is greater at 35mm than at 75mm. The histograms suggest that there is a large amount of local mixing near the valves and a smaller *large scale* rotation. This is in agreement with the Reynolds stress plots which suggested their the mixing downstream of the valves at 75 mm is less intense and more spatially uniform.

Conclusion

PIV measurements were taken in a water analog engine. A unique triggering system was implemented with a standard CCD camera. Two sets of measurements were taken at 35 mm and 75 mm downstream from the top of the cylinder at the geometric centre of the engine. An adaptive cross correlation algorithm developed by Usera (1999)

was used to validate the velocity fields. The average vorticity, Reynolds stress contours and Reynolds stress histograms indicated that there was a large degree of local mixing near the valves at 35 mm which decayed in magnitude and spread out in space further downstream at the 75 mm location. The results suggest that the interaction of the jet from the valves and the piston results in a very fast large scale mixing within this flow field. The initial jets that result front the openings between the valves and the valves and cylinder surfaces do not grow uniformly but have significant interaction.

Future work will include a statistical study of the eye validation procedure as compared to a typical moving average as well as the study of statistically significant spatial derivatives using wavelet transforms as turbulent filters.

Acknowledgements
The authors gratefully acknowledge Prof. G. Usera (IMFIA, University of the Republic, Montevideo, Uruguay) for providing the software to perform the PIV analysis. This work was supported by the Natural Science and Engineering Research Council (NSERC) of Canada.

References

Adrian, R.J. (1991) Particle-imaging techniques for experimental fluid mechanics. *Ann. Rev. Fluid Mech.* Vol. 23, pp. 261-304.

Adrian, R.J. (1997) Dynamic ranges of velocity and spatial resolution of particle image velocimetry. *Measurement Science and Technology*, Vol. 8(No. 12), pp. 1393-1398.

Amsden, A.A. (1993) KIVA-3: A KIVA Program with Block-Structured Mesh for Complex Geometries. (Tech Report LA-12503-MS). Los Alamos National Laboratory.

Ancimer, R., Sullivan, P. and Wallace, J. (2000, May), Decomposition of measured velocity fields in spark ignition engines using discrete wavelet transforms. Accepted by Experiments in Fluids.

Arcoumanis, C., Green, H. and Wong, K. (1987) Flow structure visualization in reciprocating engines. Flow Visualization IV, pp. 705-711.

Catania, A.E. and Mittica, A. (1987) Induction system effects on small scale turbulence in a high-speed diesel engine. *ASME J. of Engineering for Gas Tubines and Power*, Vol.109, pp. 491-502.

Choi, W.-C. (1998) Effects of operating speed on 3-D mean flow measured at the end of intake stroke in an {IC} engine. *JSME International Journal, Series B*, Vol. 41(No. 2), pp. 338-343.

Choi, W.-C. and Guezennec, Y.G. (1997) Experimental measurements of the spatial distribution of 3-D Lagrangian dispersion rates. *JSME International Journal, Series B*, Vol. 40(No. 4), pp. 583-591.

Choi, W.-C. and Guezennec, Y.G. (1999) Study of the flow field development during the intake stroke in an IC engine using 2-D PIV and 3-D PTV. SAE Paper No. 1999-01-0957, pp. 9-22.

Choi, W.-C., Guezennec, Y.G., Lee, C.-W., Chun, D.-C. and Chi, Y.-H.(1996) Effects of intake valve lift profile and RPM on 3-D mean and fluctuating in-cylinder flows in an IC engine. *ASME, 1996 Spring Technical Conference, ICE*-Vol. 26-2, pp. 9-14.

Davis, J. (1999). Investigation of Turbulent Flow in a Reciprocating Engine Using Particle Image Velocimetry. M.A.Sc Thesis, University of Toronto.

Denlinger, A., Guezennec, Y.G.\BCBL{} \BBA{} Choi, W.-C.(1998). Dynamic evolution of the 3-D flow field during the latter part of the intake stroke in an IC engine. *SAE Paper No. 980485*, pp. 163-173.

Dent, J.C. and Salama, N.S. (1975) The measurement of the turbulence characteristics in an internal combustion engine cylinder. *SAE Paper No. 750886*, pp. 1-12.

Durst, F., Fukui, K. and Pereira, J. (1992). Fluid dynamically caused cycle-to-cycle variations in piston-driven pipe expansion flows. *Experiments in Fluids*, pp. 1--10.

Durst, F., Maxworthy, T.,&Pereira, J. (1989). Piston-driven, unsteady separation at a sudden expansion in a tube: Flow Visualization and LDA measurements. *Phys. Fluids*, pp. 1249-1260.

Ekchian, A., & Hoult, D. (1979). Flow visualization study of the intake process of an internal combustion engine. *SAE Paper No. 790095*, pp. 1-13.

Heywood, J. B. (1988). Internal Combustion Engine Fundamentals (1 ed.). New York: McGraw-Hill.

Khalighi, B. (1990). Intake-generated swirl and tumble motions in a 4-valve engine with various intake configurations-Flow Visualization and Particle Tracking Velocimetry. *SAE Paper No. 900059*, pp. 1-21.

Khalighi, B., & Huebler, M. (1988). A transient water analog of a dual-intake-valve engine for intake flow visualization and full-field velocity measurements. *SAE Paper No. 880519*, pp. 1-15.

Kumar, S., & Banerjee, S. (1998). Developement and application of a hierarchical system for digital particle image velocimetry to free-surface turbulence. *Physics of Fluids*, Vol. 10 (No. 1), pp. 160-177.

Lancaster, D. (1976). Effects of engine variables on turbulence in a spark-ignition engine. SAE Paper No. 760159, pp. 1-18.

Li, W., & Sullivan, P. (2000). Computational investigation of reciprocating flow in a water engine. For presentation at Flucome 2000, Sherbrooke, QC.

Liou, T.-M., & Santavicca, D. A. (1983). Cycle resolved turbulence measurements in a ported engine with and without swirl. *SAE Paper No. 830419*, pp. 1-13.

Nogueira, J., Lecuona, A., & Rodriguez, P. A.(1997). Adaptive algorithms for PIV image analyzing. *Measurement Science and Technology*, Vol. 8, pp. 1493-1501.

Raffel, R., Willert, E., & Kompenhans, J. (1998). Particle Image Velocimetry: A Practical Guide. Berlin: Springer.

Reuss, D. L., Adrian, R., Landreth, C., French, D. F., & Fansler, T. D. (1989). Instantaneous Planar Measurements of Velocity and Large Scale Vorticity and Strain Rate in an Engine Using Particle-Image Velocimetry. *SAE Paper No. 890616*, pp. 1-25.

Reuss, D. L., Bardsley, M., Felton, P., Landreth, C., & Adrian, R. (1990). Velocity, Vorticity, and Strain-Rate ahead of a Flame Measured in an Engine using Particle Image Velocimetry. *SAE Paper No. 900053*, pp. 1-17.

Sullivan, P., Ancimer, R., & Wallace, J. (1999). Turbulence averaging within spark ignition engines. *Experiments in Fluids*, Vol. 27, pp. 92-101.

Trigui, N., Choi, W.-C., & Guezennec, Y. G. (1996). Cycle resolved turbulence intensity measurement in IC engines. *SAE Paper No. 962085*, pp. 1-12.

Trigui, N., Kent, J., Guezennec, Y. G., & Choi, W.-C. (1994). Characterization of intake generated fluid flow fields in IC engines using 3-D Particle Tracking Velocimetry (3-D PTV). *SAE Paper No. 940279*, pp. 1-12.

Usera, G. (1999). Adaptive algorithms for PIV image analyzing. Grupo de Trabajo Sobre Hidromecanica 5, 11-14 May 1999.

Westerweel, J. (1993). Digital particle image velocimetry: theory and application. Ph.D. Thesis, Technical University of Delft.

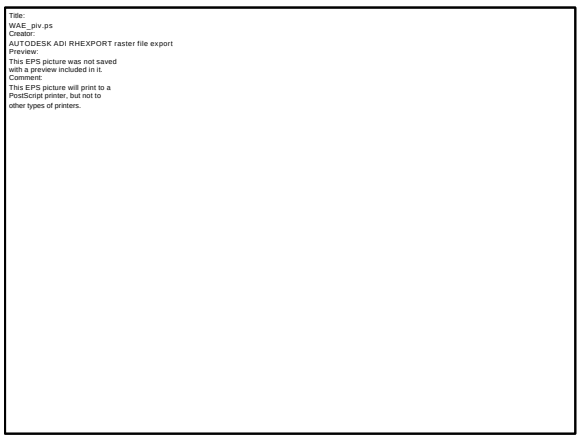

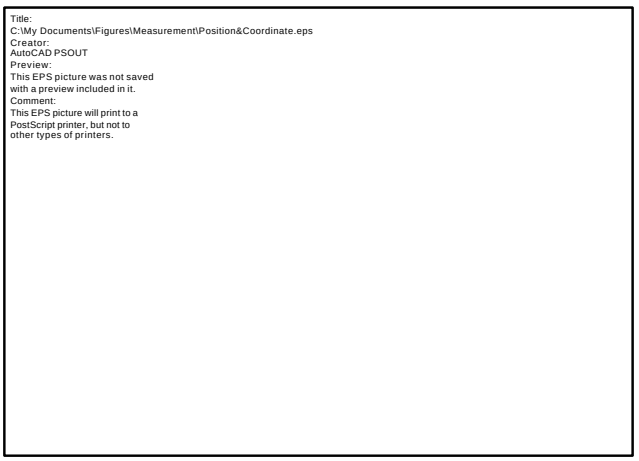

a) PIV system and water analog engine

b) Measurement Positions and coordinates

Figure 1: Experimental details

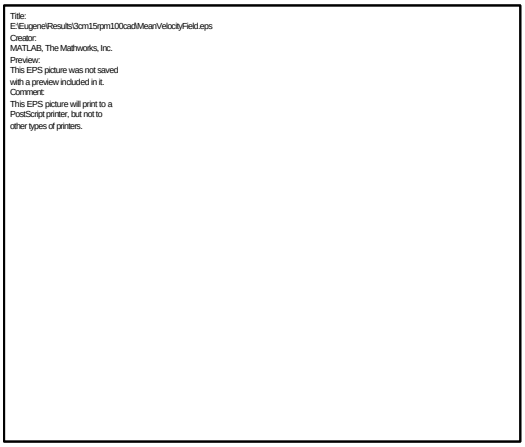

a) Mean velocity field (35 mm)

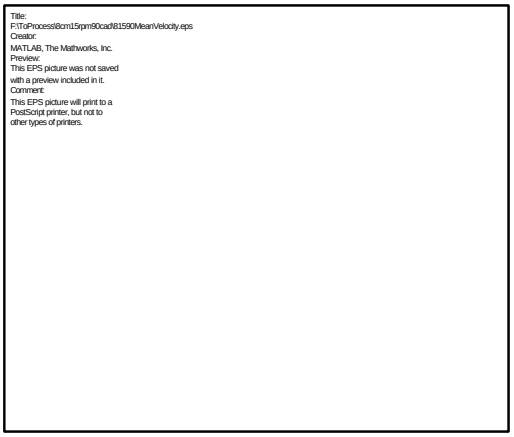

b) Mean velocity field (75 mm)

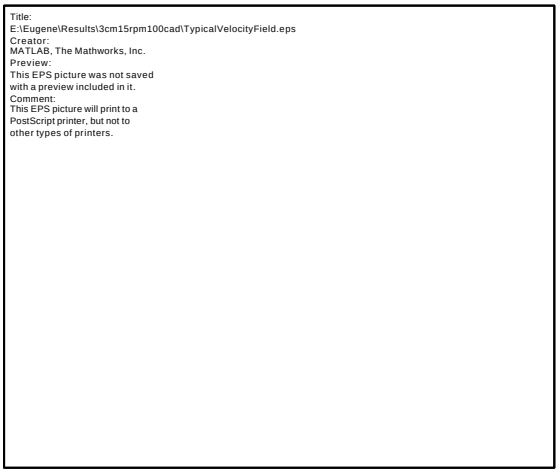

c) Instantaneous velocity field (35 mm)

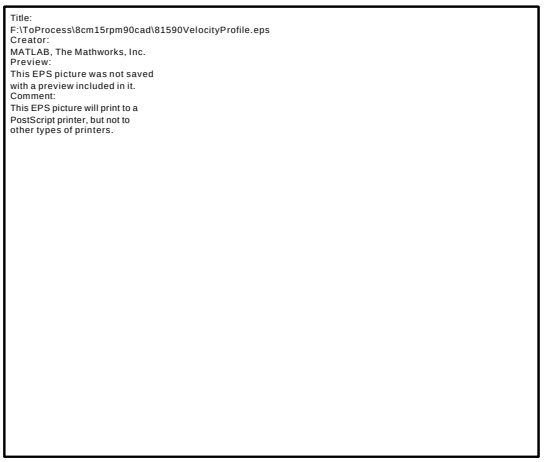

d) Instantaneous velocity field (75 mm)

Figure 2: Velocity fields; 35 and 75 mm downstream, 90 CAD ATDC, and 15 RPM

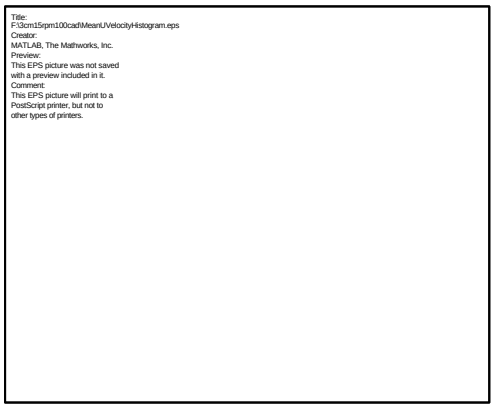

a) Histogram of mean U velocity (35 mm)

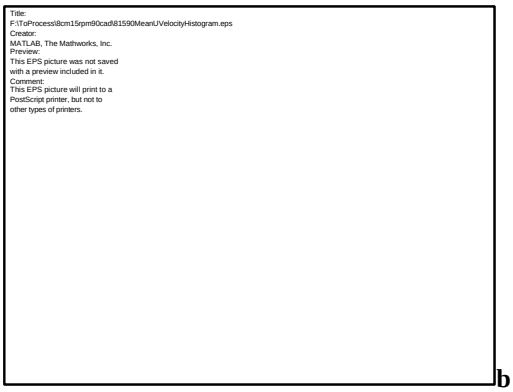

b) Histogram of mean U velocity (75 mm)

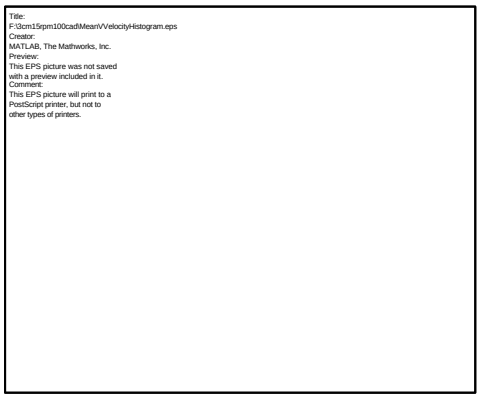

c) Histogram of mean V velocity (35 mm)

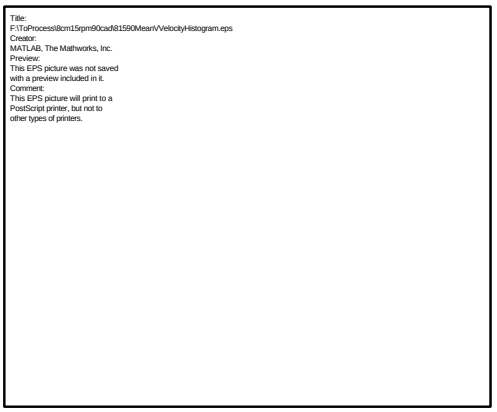

d) Histogram of mean V velocity (75 mm)

Figure 3: Mean Velocity Histograms (35 and 75 mm), 90 CAD ATDC and 15 RPM

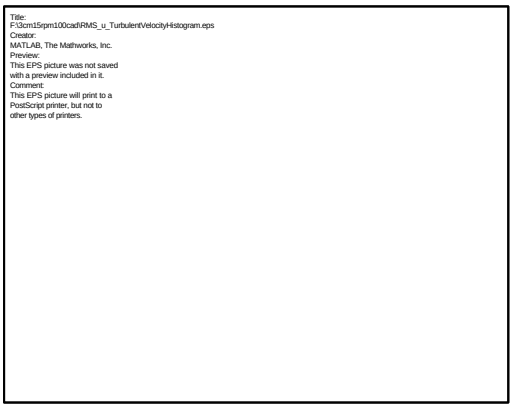

a) Histogram of u' (35 mm)

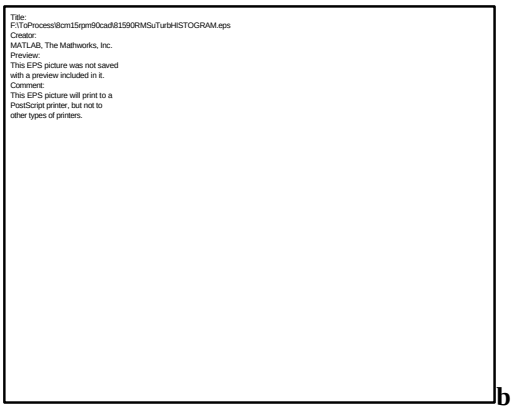

b) Histogram of u' (75 mm)

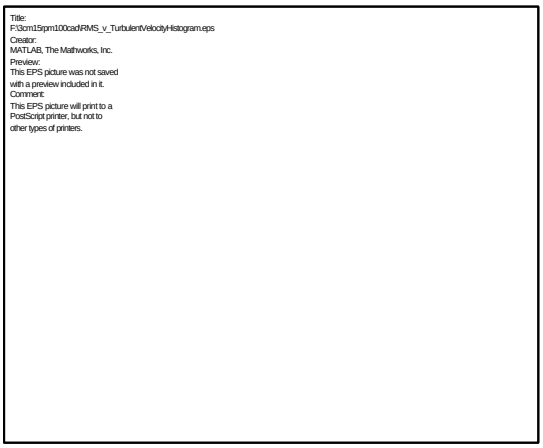

c) Histogram of v' (35 mm)

d) Histogram of v' (75 mm)

Figure 4: u’ and v’ Histograms (35 and 75 mm), 90 CAD ATDC and 15 RPM

a) Reynolds stress <u'u'> (35 mm)

b) Reynolds stress <u'u'> (75 mm)

c) Reynolds stress <v'v'> (35 mm)

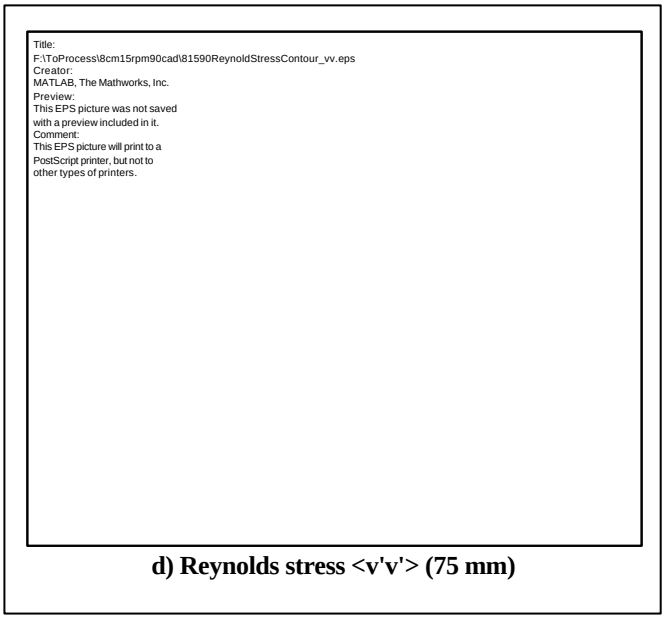

d) Reynolds stress <v'v'> (75 mm)

Figure 5: Reynolds stresses (u'u' and v'v') (35 and 75 mm), 90 CAD ATDC and 15 RPM

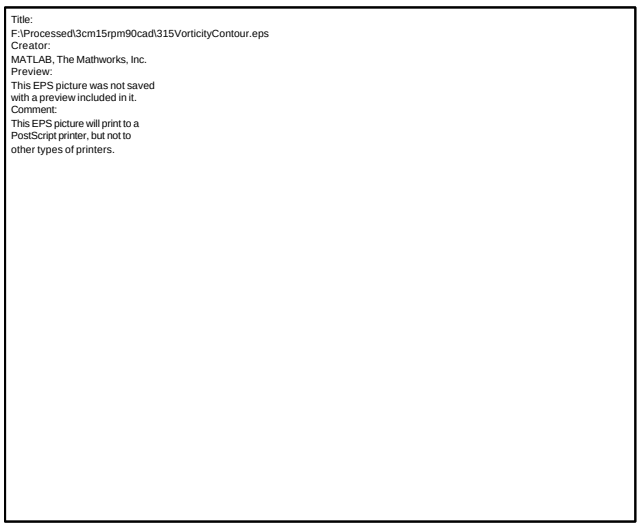

a) Mean vorticity (35 mm)

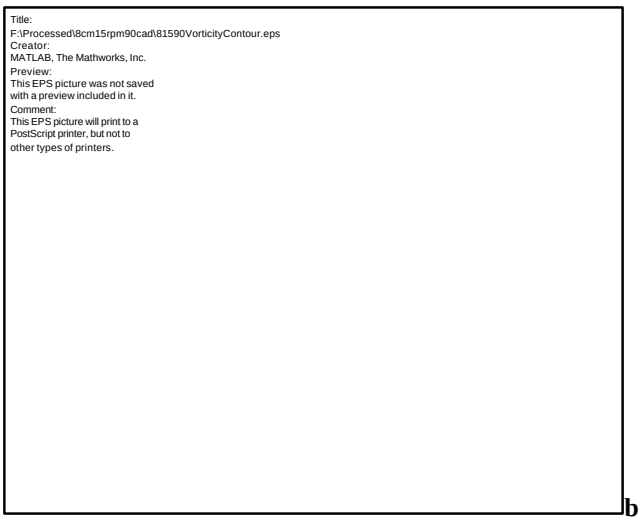

b) Mean vorticity (75 mm)

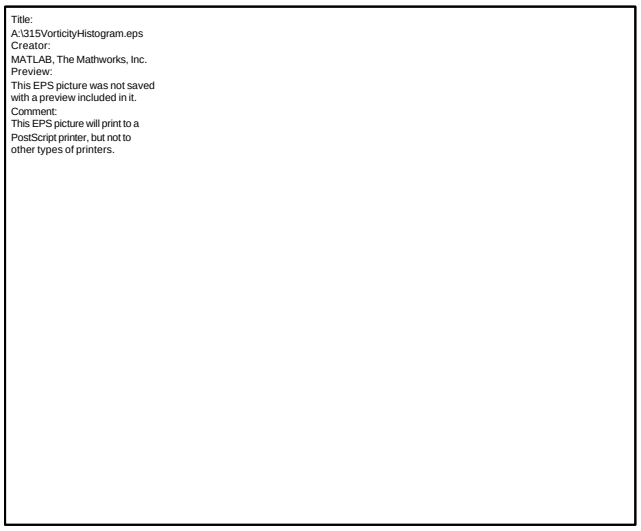

c) Mean vorticity histogram (35 mm)

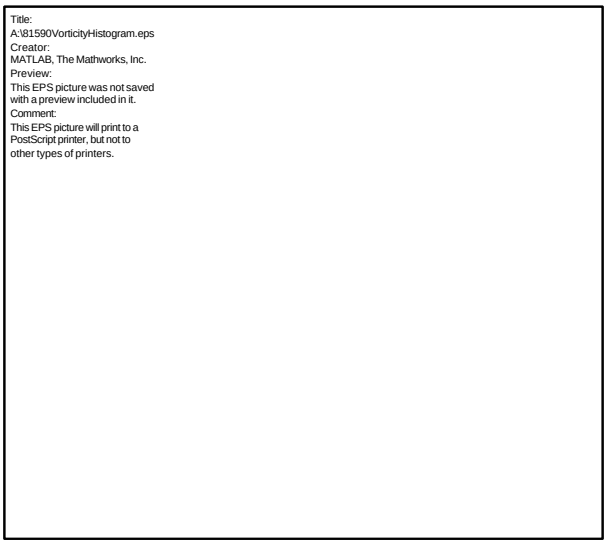

d) Mean vorticity histogram (75 mm)

Figure 6: Mean vorticity (35 and 75 mm), 90 CAD ATDC and 15 RPM